Structural and Magnetic Characterisations of Pb-Doped MgO Nanoparticles by a Modified Pechini Method

Structural and Magnetic Characterisations of Pb-Doped MgO Nanoparticles by a Modified Pechini Method

Israa A.Najem[1,4], Shaker J. Edrees[2], Fadhil Abd Rasin[3]
[1] Department of Materials Engineering, University of Technology, Baghdad, Iraq.
[2] Department of Ceramic & Building Materials Engineering, College of Materials Engineering, University of Babylon, Babylon, Iraq.

[3] Department of Materials Engineering, University of Technology, Baghdad, Iraq.
[4] University of Al-Furat Al-Awsat Technical University, Babylon Technical Institute, Babylon, Iraq.
*corresponding author: israadnan2000@gmail.com

Abstract. Doping magnesium oxide nanoparticles (MgO-NPs) forms a good material for magnetisation applications. The Room Temperature Ferromagnetic (RTFM) of Pb^{2+}-doped ions MgO-NPs synthesised by a modified Pechini method are discussed in the present paper. The structural, morphological and magnetic properties of the samples were characterised by X-ray diffraction (XRD), Field Emission scanning electron microscopy (FE-SEM), Energy Dispersive Spectroscopy (EDS) and vibrating sample magnetometer (VSM).
The XRD results showed that the synthesised materials have a single set of peaks in the XRD patterns, corresponding to the cubic phase of MgO-NPs. As the Pb content increased in the host MgO-NPs leading to an increase in the lattice parameter, the interplanar spacing and the crystallite size; however, the intensity decreased.
Small spherical nanoparticles (22.87–29.05nm) were observed in the Pb^{2+}-doped ions MgO samples by (FE-SEM). The purity of the samples was confirmed using EDS spectroscopy.
The pure MgO and doped samples exhibiting RTFM may be attributed to vacancy defects, which caused local magnetisation. The saturation magnetism (Ms) was found to be varied as a function of doping concentration. The maximum (Ms) was found at x=0.015 of $Mg_{0.985}Pb_{0.015}O$ sample. The obtained results suggest that both Pb doping and oxygen vacancies play an important role in the development of room-temperature ferromagnetism.

Keyword: doping, MgO-NPs, PbO, Pechini, RTFM, VSM

1. Introduction

The study and development of nanomaterials and nanostructures are a key ambition in making the industry more innovative and more competitive. Nanomaterials and nanostructures perform a very important supporting function for applications, mainly for providing a notable surface-area-to-volume ratio than conventional structures [1][2][3].
Metal oxide nanoparticles are another field of nanoparticles (NPs), which can be directly used in the application of common chemical reactions, with special electronic and magnetic properties allowing them to be applicable in specific areas [4], such as TiO_2-NPs [5], ZnO-NPs [6], Fe_2O_3-NPs [7] and MgO-NPs [8].
Among these oxides, magnesium oxide nanoparticles with sodium chloride structure have attracted the attention of several researchers due to their exceptionally functional materials that have been widely utilised in superconductors [9], antibacterial materials [10] and magnets [11].

Doping magnesium oxide nanoparticles is an important tool for a wide variety of modifications, with the dopant impurities affecting the properties of metal oxide nanoparticles, such as [12] the optical properties when Zn^{+2}-doped ions affect MgO [13][14], in that the band gap of a MgO lattice, when occupied by transition ions (Ti-, Cr-, Fe-, Ni-, Zn), which can play an important role in plasma display panels [15], the magnetic properties of MgO nanoparticles are modified by doping Mn^{+2} ions [16]**,** and the magnetic field can depend on the thermal conductivity of Fe^{+3} ions doping MgO [17]. The antibacterial activity can markedly be promoted with Ag-doped MgO nanoparticles [18], and the luminescence intensity is greatly enhanced according to the increase of Eu^{3+} concentrations in a MgO lattice [19].
Many researchers note that a bulk rocksalt structure (MgO, HfO, CaO and Al2O3) is nonmagnetic, while their nanoparticle structure confirms room-temp ferromagnetism (RTFM) [20][21]. Hence, the origin of magnetism in MgO-NPs is an issue of some recent interest [22][23] because the rocksalt structure does not include ions with partially filled d or f bands, since the valence band is controlled by O-2p orbitals, and there are no valence d electrons in the rocksalt structure [24][25][26]. Consequently, such magnetisation does not demand the existence of free carriers [27], but it can be correlated with the presence of a slight concentration of intrinsic point defects, isolated cation vacancies, leading to the formation of a high-spin defect site, which can form local magnetism in MgO-NPs [24][25].
Several preparation routes have been involved in preparing a pure and doped MgO-NPs, such as combustion [28], aerogel route [29], hard templating pathway [30], microwave sol-gel method [31], liquid-phase method [32], co-precipitation [33], green synthesis [34], sol-gel method [18], modification of a Pechini sol–gel process [35] and a spinning disk reactor [36].
Among the overall number of the chemical synthesis methods obtained in the preparation of pure and doped MgO-NPs, the Pechini method was a favourite selection due to its main role in the synthesis of magnetic materials, high-temperature superconductors, ceramics and catalysts [37]. The preference for this method includes good stoichiometric control, good homogeneity and good control of particle morphology [38].
The main objective of this work is to detect the influence of Pb^{2+} ions as incorporated into the crystal structure of MgO-NPs nanoparticles, where the samples were prepared by a modified Pechini method. In order to obtain a better understanding of the current work, the XRD, FE-SEM coupled with EDX and VSM tests were investigated to examine changes that take place in the structure with an increase in the fraction of doping.

2. Experimental Method

2.1 Chemicals Used

Magnesium nitrate hexahydrate ($Mg(NO_3)_2 \cdot 6H_2O$) [BDH Chemicals Ltd, England, > 99% purity], lead nitrate ($Pb(NO_3)_2$) [Chemicals PVT, India, > 99% purity], citric acid ($C_6H_8O_7.H_2O$) [CDH, India, >99%], Ethelyen Glygol, EG, ($CH_2(OH).CH_2OH$) [Chemicals PVT. LTD, India, > 99% purity] and distilled water were involved to prepare ($Mg_{1-x}pb_xO$)-NPs samples, where x=(0,0.005,0.01,0.015, 0.02,0.025,0.03), using a modified Pechini method. All raw chemical materials were used without any further purifications.

2.2 Samples Preparation

2.2.1 Synthesis of MgO-NPs Nanoparticles.

The procedure of synthesised MgO-NPs involved the preparation of a stable aqueous solution of the metal salt starting with the magnesium nitrite solution, and the tricarboxylic acid as citric acid solution were dissolved separately in an adequate amount of deionised water (100ml) for each of them, in a molar ratio of 1:1 and stirred for one hour under constant stirring (FALC instrument-F91). Then, citric acid was added into a magnesium nitrite solution to chelate Mg^{2+} ions in the solution; the resulting solution was kept at 90°C for three hours under constant stirring. EG was added with fixed mass ratio, CA/EG, 2:3. The colour of the final mixed solution gradually changed into a yellow shade as a result of water

evaporation. Finally, a very viscous gel formed with a brown colour. The dehydrated gel was calcinated at a moderate temperature of 420°C for two hours with 3℃ /min as a heating rate using a furnace device (PIF 160/15- Made in Turkey) to form a loose powder.
The procedure of the synthesised ($Mg_{1-x}pb_xO$)-NPs samples, where x=(0–0.03), involved the preparation of an extra stable aqueous solution of lead nitrite, dissolved separately in an adequate amount of deionised water under constant stirring for one hour. The citric acid was added into mixed solutions of the magnesium nitrite and lead nitrite to chelate Mg^{2+} and Pb^{2+} in the solution. The same procedure steps were repeated for the preparation of MgO-NPs samples to obtain ($Mg_{1-x}pb_xO$)-NPs samples.

3. Characterisation techniques

All the seven samples of ($Mg_{1-x}pb_xO$)-NPs were analysed by powder XRD, FE-SEM coupled with EDS analysis and VSM. Powder X-ray diffraction patterns were obtained using a Shimadzu-6000 diffractometer with Cu-Kα radiation (λ=1.5406Å). The surface morphologies of the nanoparticles samples were investigated using a field emission scanning electron microscope (TESCAN MIRA3 FEG-SEM) operating at 30kV coupled with an energy-dispersive spectroscopy (EDS) facility for elemental analysis. The magnetic measurements were carried out using a vibrating sample magnetometer (VSM) type cryogenic device at room temperature.

4. Result and Discussion

4.1 *Structural Analysis X-ray diffraction (XRD)*

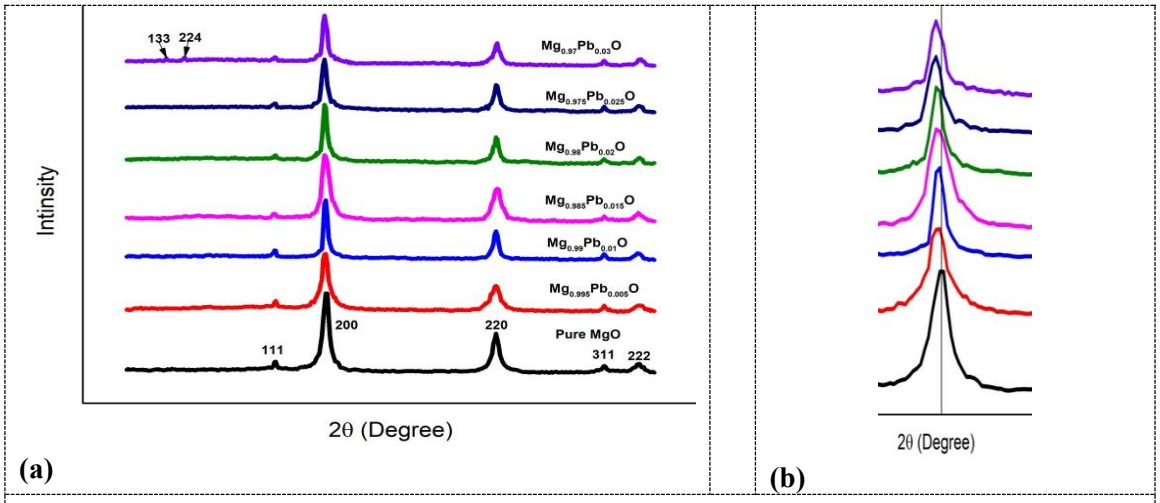

Figure 1. XRD analysis for ($Mg_{1-x}pb_xO$)-NPs samples (a) XRD pattern for ($Mg_{1-x}pb_xO$)-NPs samples calcined at 420°C for 2 hours. (b) XRD shifting for pure and doped ($Mg_{1-x}pb_xO$)-NPs samples.

For characterising crystalline materials, a powerful non-destructive technique was performed to provide information on phases, structures, preferred crystal orientations and other structural parameters, such as crystallinity, width, average grain size and the intensity of the diffraction peaks, which depend on lattice strain. The powder of the prepared ($Mg_{1-x}pb_xO$)-NPs samples using a modified Pechini method were calcined at 420°C for two hours, investigated via XRD technique.
Figure 1a reveals the reflections resulting from the ($Mg_{1-x}pb_xO$)-NPs samples. The pure MgO-NPs and all the doped samples are indexed well to the cubic phase with Fm3m (#225) as a space group.
However, the pure MgO-Nps sample showed five major diffraction peaks at positions 36.6325, 42.6868, 61.9761, 74.3027 and 78.2192. The corresponding lattice planes were (111), (200), (220), (311) and (222), which can be matched with [ICSD PDF code 01-075-0447]. These results are in line with earlier reports[16][18].

However, the XRD pattern for the $Mg_{0.97}Pb_{0.03}O$ sample appears as an additional weak peak, coinciding with PbO oxide. The strange peaks appear at positions 24.49 and 26.60, corresponding to the lattice planes 133 and 224 respectively, which were matched with [ICSD PDF (no. 45-964)].

The appearance of the strange PbO peaks can be attributed to the hardness of doping Pb^{+2} ions with a high concentration, due to differences in the ionic radius between Pb^{2+} (1.19 Å) ions and Mg^{2+} (0.72 Å) ions. So, the extra amount of Pb^{+2} ions can be segregated as a metal oxide phase (PbO) on the grain and at the grain boundaries of MgO-NPs host lattice [39]. This denotes that at or upward of this doping concentration of x=0.03 and under current experiential conditions, the Pb^{2+} ions cannot be inserted in the lattice sites. However, the additional amount of Pb^{2+} ions existing in an MgO solid solution can undergo oxidation to PbO [40]. Therefore, in the present research, the solubility boundary of Pb^{2+} ions in the MgO host lattice was about 0.005–0.03.
The strongest diffraction peak (200) for the pure structure of MgO-NPs is positioned at (42.6868), while for the doped samples are observed shifting to a lower 2θ peaks position, as cleared in Figure1.b.
Such increasing in shifting can be ascribed to the ionic radius difference between Pb^{2+} ions and Mg^{2+} ions that incorporated in the MgO host lattice.
The shifting of $Mg_{0.97}Pb_{0.03}O$ sample shows disorder shifting due to the incorporation of small fractions of the Pb^{2+} ions in the host lattice and the extra fraction separated as PbO oxide.
The interplanar d-spacing increases from (x=0–0.025) due to increased strain in the lattice of compounds, while it decreases at (x=0.03) doping due to the formation of the PbO phase [14][18]. Table 1 shows the values of d-spacing of pure and doped samples.
It is also evident from Figure 1b that the diffraction peaks shift lightly in this position, indicating a light change in the lattice parameter. Such changing leads to a contraction or expansion in the lattice due to the introduction of a dopant with a different ionic radius in the host lattice. A variation of the lattice constant was proportional to the difference between the ionic radius of the dopant, substituted host lattice atom and the concentration of the dopant [41]. According to Table 1, the lattice parameter for pure MgO-NPs is equal to (4.22832Å), while it is increased for doped samples. The maximum increase in the lattice parameter is (4.22983Å) at (x=0.025) for the $Mg_{0.975}Pb_{0.025}O$ sample.
However, the lattice parameter of the $Mg_{0.97}Pb_{0.03}O$ sample at (x=0.03) is decreased. Such a decrease can be attributed to the formation of the secondary phase of PbO oxide [18][40].
It is also evident from Figure 1b when Pb^{2+} ions were doped in the MgO-NPs host lattice. The intensity of the strongest diffraction peak (2θ=42.643468) along the (200) plane is decreased, and the full width at half maximum (FWHM) is increased. This indicates that the doped samples successfully replaced the Mg^{2+} ions with the Pb^{2+} ions in the MgO-NPs host lattice, and the undoped sample had a better phase purity and crystallinity since the intensity of the XRD peaks can be affected by the composition including occupancy of atomic sites, the scattering ability of constituent atoms, and fractional coordinates[18][42][43].
The average crystallite size (D) was evaluated using Scherrer's formula for the pure and doped MgO-NPs samples along (220) and (200) planes [44].

$$D = \frac{K\lambda}{\beta cos\theta} \dots\dots\dots\dots (1)$$

where D is the crystallite size, λ the X-ray wavelength of the copper anode (1.5406Å), k the shape factor (k = 0.9), β the full width at half maximum (FWHM) of the diffraction peaks, and θ the Bragg diffraction angle [45].
As the diffraction factor of Pb^{2+} ions increased, the average crystallite size (D) along (220) and (200) planes increased for the first six samples due to facilitating the crystalline growth and crystallisation of MgO-NPs, while it decreased for the $Mg_{0.97}Pb_{0.03}O$ sample, as shown in Table 1.

Table 1. Structural Parameters of Pure and Doped MgO-NPs Calcined at 420°C.

Samples	Space group	Crystalline size along(200) and (220) planes	Lattice parameter Å	d space
MgO-NPs	#225	5.693325	4.22832	2.11949
$Mg_{0.995}Pb_{0.005}O$	#225	5.696727	4.22837	2.11956
$Mg_{0.99}Pb_{0.01}O$	#225	5.91245	4.22848	2.11999
$Mg_{0.985}Pb_{0.015}O$	#225	6.412056	4.22979	2.12026
$Mg_{0.98}Pb_{0.02}O$	#225	10.12461	4.22981	2.12038
$Mg_{0.975}Pb_{0.025}O$	#225	10.24802	4.22983	2.12088
$Mg_{0.97}Pb_{0.03}O$	#225	9.27065	4.22852	2.11952

4.2 Morphology Analysis

The field emission scanning electron microscope (FE-SEM) technique was employed to explore the size and the distribution of all the samples. The images are shown in Figures 2, 3, 4, 5, 6, 7 and 8 – a for synthesised ($Mg_{1-x}pb_xO$)-NPs samples by using the modified Pechini method. The images display the agglomeration of the spherical nanoparticles, which occurs due to the high surface energy of the nanoparticles. The capability to produce agglomeration is very strong, which increases the collision frequency between particles that lead to a higher degree of agglomeration. Chemical bonds may form between particle surfaces as van der Waals forces, which are always present. Additionally, the magnetic dipole forces can potentially participate in internal particle forces[46][47].

The average grain size for all seven samples under investigation is in the (22.87–29.05nm) range, as evident in the histogram in the Figures 2, 3, 4, 5, 6, 7 and 8 – b. Grain size increases with increases in the concentricity of the Pb^{2+} ions, which is in a good convention with the crystallite size as determined from the XRD and statically histogram.

4.2 *Energy-dispersive X-ray spectroscopy EDS*

In order to confirm the composition of the prepared nanocrystals samples, the energy dispersion spectroscopy (EDS) analysis was coupled with the FE-SEM. EDS is a very useful technique for qualitative and quantitative analysis of the relative concentration of an element [48]. EDS spectroscopy, which was used to detach pure and doped MgO-NPs as shown in Figures 2, 3, 4, 5, 6, 7 and 8 – c, is capable of producing elemental distribution maps.

The EDS spectrum specified the presence of magnesium (Mg) and oxygen (O) as the only elements in the MgO-NPs sample that demonstrate high purity of the nanopowder synthesis by the modified Pechini method. It is obvious from chemical mapping that the results for pure MgO-NPs of the Mg/O atomic ratio coincide well with that of the corresponding XRD data and the bulk ratio. A partially higher oxygen atomic ratio compared to that of magnesium is possibly because of moisture absorption from the environment [49].

The EDS analysis of the doped ($Mg_{1-x}pb_xO$)-NPs samples in Figures 2, 3, 4, 5, 6, 7 and 8 – c confirm the presence of Mg, Pb and O as the only elementary components, with the absence of any extra element. The weight percentages are almost equal to their nominal stoichiometry by experimental error.

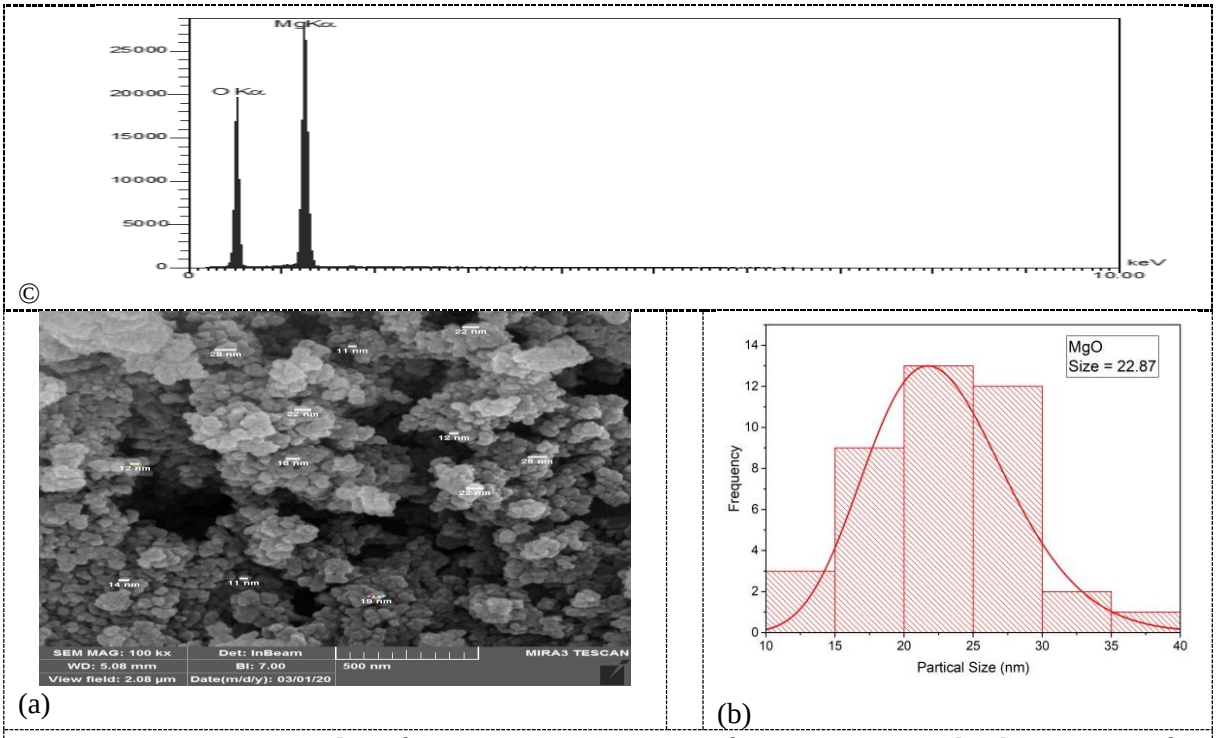

Figure 2. FE-SEM test analysis for MgO-NPs. (a) FE-SEM for MgO-NPs sample. (b) Histogram for MgO-NPs sample. (c) EDS for MgO-NPs sample.

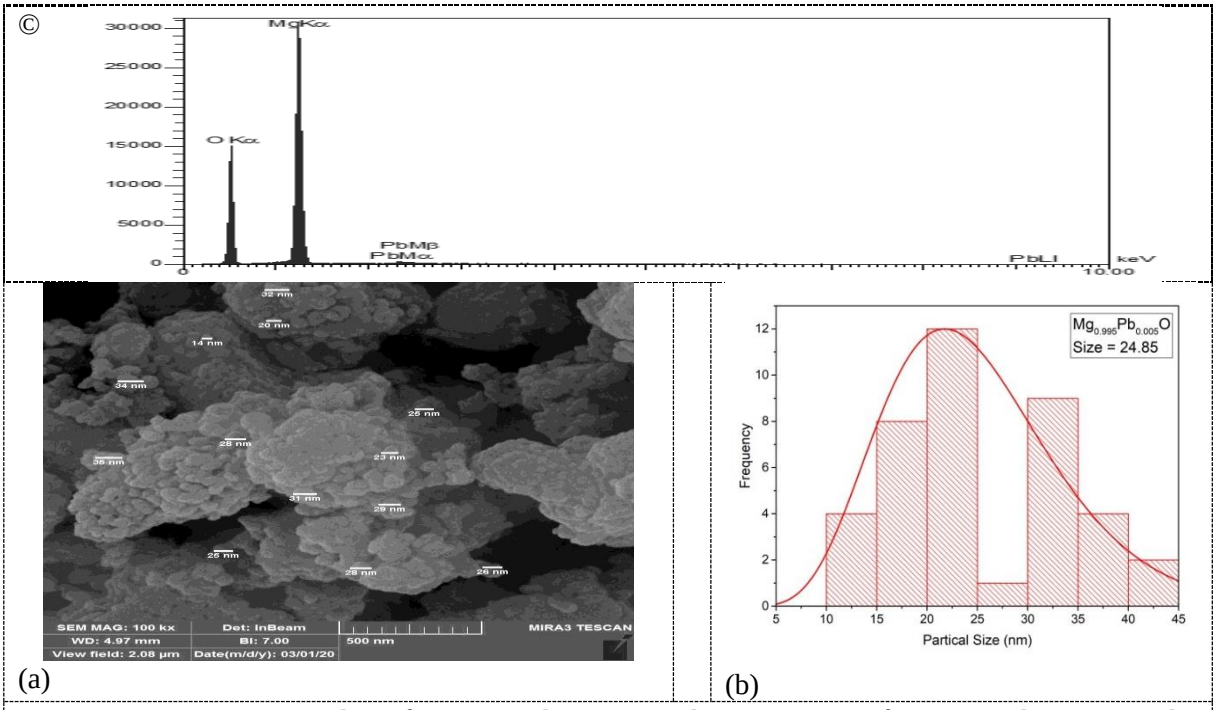

Figure 3. FE-SEM test analysis for $Mg_{0.995}Pb_{0.005}O$ sample. (a) FE-SEM for $Mg_{0.995}Pb_{0.005}O$ sample. (b) Histogram for $Mg_{0.995}Pb_{0.005}O$ sample. (c) EDS for $Mg_{0.995}Pb_{0.005}O$ sample.

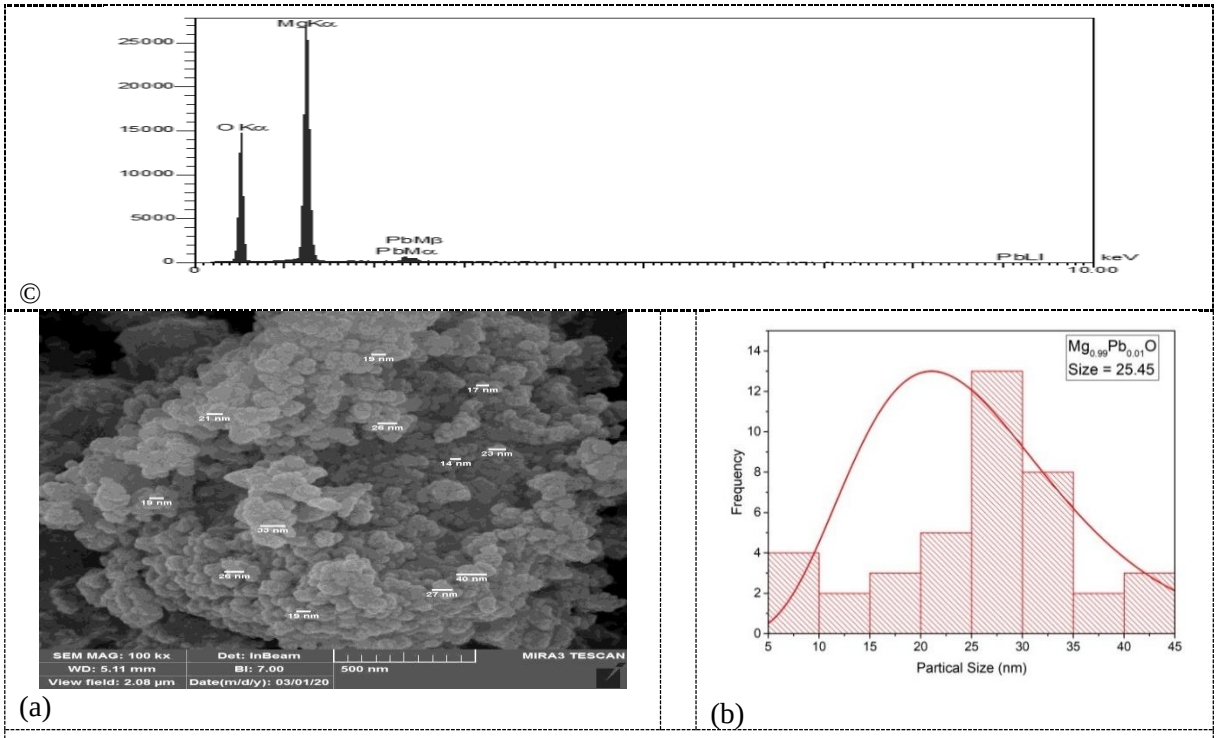

Figure 4. FE-SEM test analysis for $Mg_{0.99}Pb_{0.01}O$ sample. (a) FE-SEM for $Mg_{0.99}Pb_{0.01}O$ sample. (b) Histogram for $Mg_{0.99}Pb_{0.01}O$ sample. (c) EDS for $Mg_{0.99}Pb_{0.01}O$ sample.

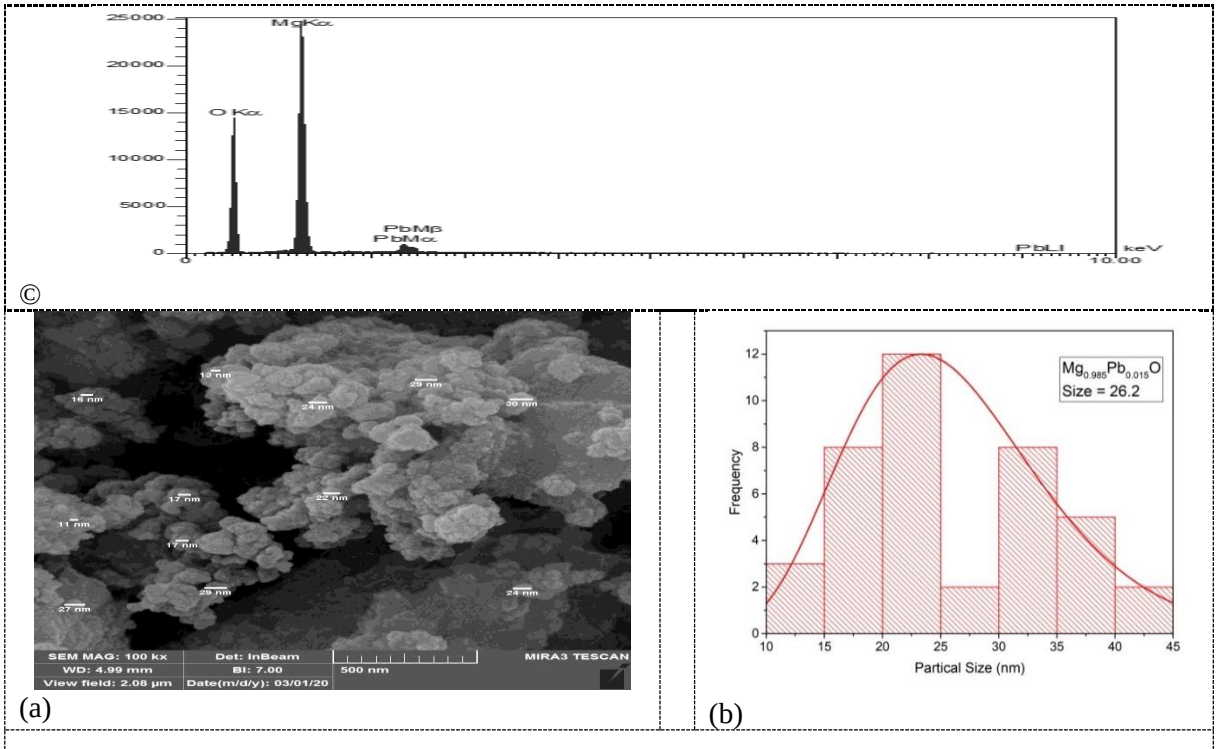

Figure 5. FE-SEM test analysis for $Mg_{0.985}Pb_{0.015}O$ sample. (a) FE-SEM for $Mg_{0.985}Pb_{0.015}O$ sample. (b) Histogram for $Mg_{0.985}Pb_{0.015}O$ sample. (c) EDS for $Mg_{0.985}Pb_{0.015}O$ sample.

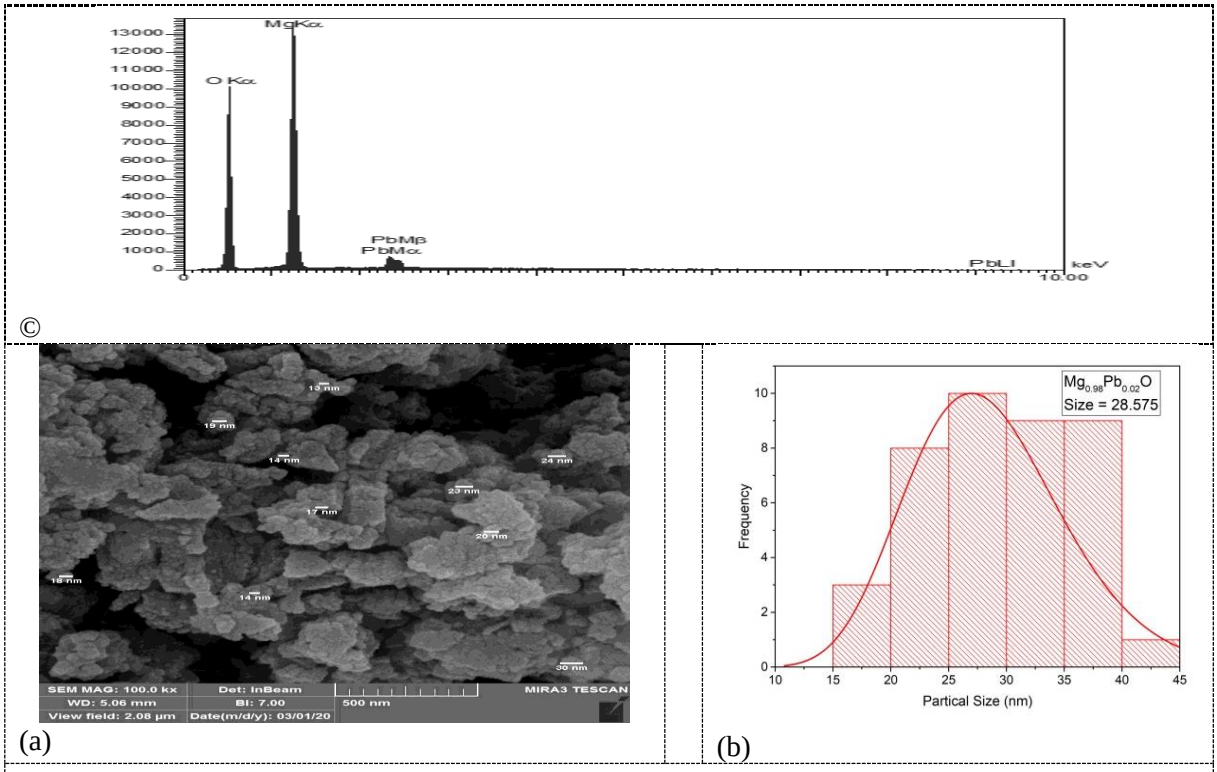

Figure 6. FE-SEM test analysis for $Mg_{0.98}Pb_{0.02}O$ sample. (a) FE-SEM for $Mg_{0.98}Pb_{0.02}O$ sample. (b) Histogram for $Mg_{0.98}Pb_{0.02}O$ sample. (c) EDS for $Mg_{0.98}Pb_{0.02}O$ sample.

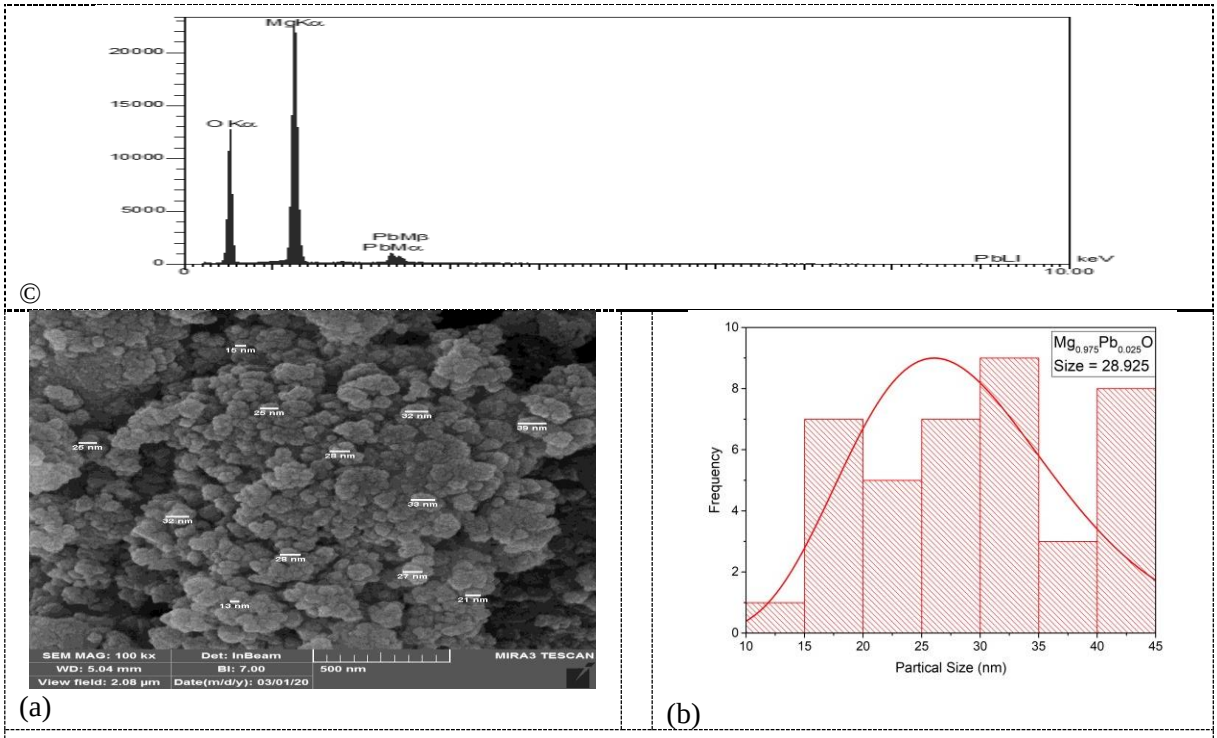

Figure 7. FE-SEM test analysis for $Mg_{0.975}Pb_{0.025}O$ sample. (a) FE-SEM for $Mg_{0.975}Pb_{0.025}O$ sample. (b) Histogram for $Mg_{0.975}Pb_{0.025}O$ sample. (c) EDS for $Mg_{0.975}Pb_{0.025}O$ sample.

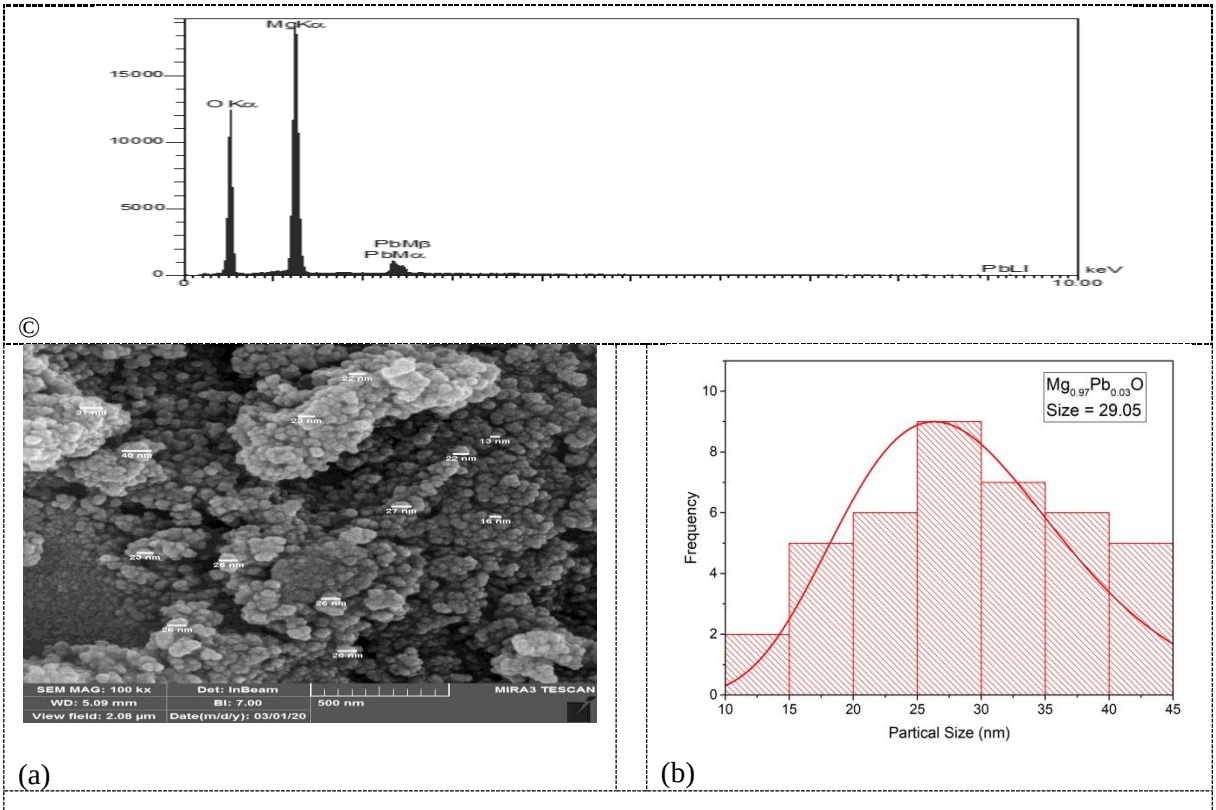

Figure 8. FE-SEM test analysis for $Mg_{0.97}Pb_{0.03}O$ sample. (a) FE-SEM for $Mg_{0.97}Pb_{0.03}O$ sample. (b) Histogram for $Mg_{0.97}Pb_{0.03}O$ sample. (c) EDS for $Mg_{0.97}Pb_{0.03}O$ sample.

4.4 VSM magnetisation

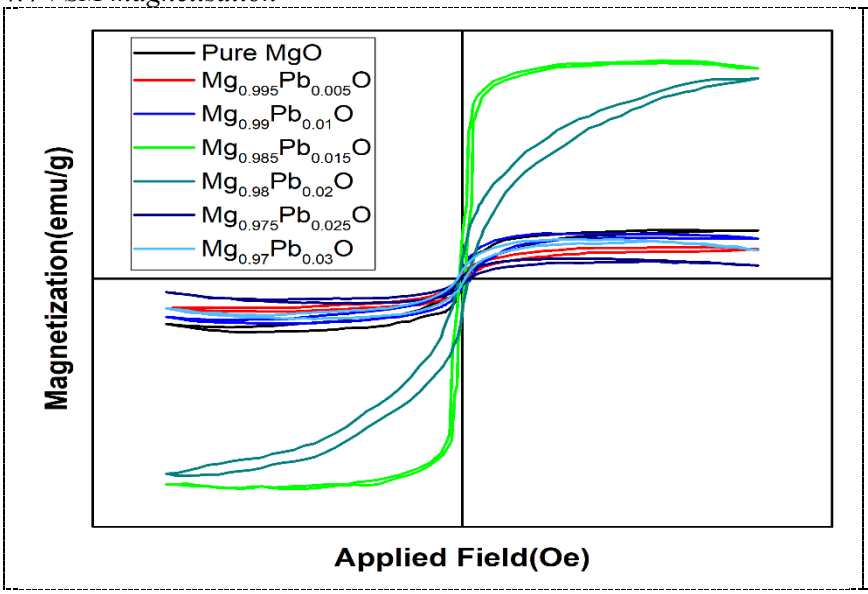

Figure 9. VSM analysis for $(Mg_{1-x}pb_xO)$-NPs samples calcined at 420°C for two hours.

The magnetisation behaviour curves for the prepared nanocrystallites $(Mg_{1-x}pb_xO)$ samples were created by modifying the Pechini method and calcined at 420°C for two hours, as plotted in Figure 9. The samples were investigated by vibrating samples magnetometer (VSM). The VSM shows the hysteresis loops for the seven samples examined at room temperature and motivated by defects.
Magnetisation in the pure and doped samples was achieved due to small crystallite size and particle size as evident from XRD and FE-SEM, respectively. The necessary conditions to achieve magnetic order

in the lattice of the pure and doped MgO-NPs samples was provided by a certain density of vacancies. Such vacancies or other defects in the lattice were achieved by nearly localised magnetic moments [50]. Such vacancies in the MgO-NPs sample are responsible for magnetisation. In addition, the vacancies were usually labelled as F,V centres, corresponding to a missing oxygen atom or Mg atom in the host lattice of MgO-NPs, respectively [51]. The reason behind the encouraging magnetic moment was the spin polarisation of 2p electrons of O atoms close to the negative charge VMg [20][25]. However, the cations were enclosed by an octahedron of anions with filled valence p bands, and the bonding anion p orbitals with lobes pointing to the cation site would be the generality energetically favoured attraction orbitals to provide the holes. Hence, holes were necessary to charge the recompense by a cation vacancy at the centre of such an octahedron [21][52].

The ferromagnetism in MgO-NPs appeared not only as a result of the VMg but also from the distribution or placement of the vacancies[20]. As Mg^{+2} ions were replaced by Pb^{+2} ions, the saturation magnetisation (Ms) was noted as varying. Such variation was due to the formative localised magnetic moment, which can occur as a result of introducing a cation defect in the MgO-NPs host lattice by doping.

According to Figure 9, the (Ms) decrease for the samples $Mg_{0.995}Pb_{0.005}O$ and $Mg_{0.99}Pb_{0.01}O$ as compared to the pure MgO-NPs sample due to an increase in the crystallite size and particle size, as cleared from XRD and FE-SEM. The magnetisation of $Mg_{0.995}Pb_{0.005}O$ and $Mg_{0.99}Pb_{0.01}O$ are close to a paramagnetic nature. Such magnetisation can occur due to the exchange of one ion with another ion, leading to the reproduction of holes in dopant 2p orbits and the formation of a local magnetic moment on the oxygen sites. Hence, the magnetic moment is a transfer of atoms without d- or f- electrons [25][53]. Consequently, it was convenient to assume that the observed magnetic signal was relative to the vacancies' density [53][54]. Thus, the excessive cation vacancies by doping are expected to change the observed magnetic signal.

The typical magnetisation appears in the $Mg_{0.985}Pb_{0.015}O$ sample, which has a symmetric hysteresis loop, which can be attributed to comparable nanoparticles size and associated with cation inversion [55]. This may happen due to the total replacement of vacancies by cation in a typical situation with an identical localised moment. The $Mg_{0.98}Pb_{0.02}O$ sample has S-shape hysteresis, suggesting superparamagnetic. In the $Mg_{0.975}Pb_{0.025}O$ and $Mg_{0.97}Pb_{0.03}O$ samples, the (Ms) begin to decrease as compared to $Mg_{0.985}Pb_{0.015}O$ due to an increase in the fraction of cations in the lattice by doping. Such an increase leads to the distorting of the lattice structure and a decrease in the localised magnetic moment; moreover, the decrease in the (Ms) of the $Mg_{0.97}Pb_{0.03}O$ sample was due to a separation of a small fraction of Pb^{2+} ions as PbO oxide, as clarified from XRD.

5. Conclusions

Pb^{+2}-doped MgO nanoparticles samples have been successfully synthesised via a modified Pechini method. The calcination temperatures were used 420°C for two hours with 3°C /min as a heating rate to prepare pure and $(Mg_{1-x}pb_xO)$-NPs-doped samples with Pb^{+2} concentrations varying from x=0.05-0.03. The substituted hydroxide precursors have been demonstrated as being effective for the synthesis of Pb^{+2}-doped MgO nanoparticles as they can provide good homogeneity. Powder XRD results confirmed the formation of a single cubic phase with space group Fm3m (#225). As a result of increasing the fraction of doping, the strongest diffraction peak (200) has shifted towards less 2θ values, and the interplanar d-spacing, lattice parameter and crystallinity have been increased. Furthermore, the intensity was reduced, which can be attributed to the ionic radius difference between Pb^{2+}(1.19 Å) and Mg^{2+} (0.72 Å) ions. The morphology surface for pure and doped nanoparticles samples showed a spherical nanoparticle shape. The average grain size increased with increasing the dopant concentration, as confirmed by statically histogram and crystallinity from XRD, which was in the range 22.87–29.05nm for pure and doped samples. The EDS confirmed the presence of Mg, Pb and O as the only elementary components, and the weight percentages were nearly their nominal stoichiometry. The RTFM was motivated by vacancy defects rather than the kind of dopant ions. The saturation magnetisation was noted as being varied, given the dopant incorporated in the host lattice of MgO-NPs. The reason behind such change was the formation of a local magnetic moment, which can vary according to the density of defect and oxygen vacancies. The maximum (Ms) was achieved when x=0.015 of the $Mg_{0.985}Pb_{0.015}O$ sample.

6. References

[1] Wang ZL. Characterization of nanophase materials. vol. 18. 2001. https://doi.org/10.1002/1521-4117(200110)18:3<142::AID-PPSC142>3.0.CO;2-N.
[2] Greim (Chairman) H. Constitution and Procedures of the Commission for the Investigation of Health Hazards of Chemical Compounds in the Work Area. 2004. https://doi.org/10.1002/3527600418.make016.pub2.
[3] Iqbal T, Tufail S, Ghazal S. Synthesis of Silver, Chromium, Manganese, Tin and Iron Nano Particles by Different Techniques. Int J Nanosci Nanotechnol 2017;13:19–52.
[4] Wang S, Gao L. Laser-driven nanomaterials and laser-enabled nanofabrication for industrial applications. Elsevier Inc.; 2019. https://doi.org/10.1016/B978-0-12-815749-7.00007-4.
[5] Wang C, Shi Z hai, Peng L, He W min, Li B liang, Li K zhi. Preparation of carbon foam-loaded nano-TiO2 photocatalyst and its degradation on methyl orange. Surfaces and Interfaces 2017;7:116–24. https://doi.org/10.1016/j.surfin.2017.03.007.
[6] Harun K, Mansor N, Ahmad ZA, Mohamad AA. Electronic Properties of ZnO Nanoparticles Synthesized by Sol-gel Method: A LDA+U Calculation and Experimental Study. Procedia Chem 2016;19:125–32. https://doi.org/10.1016/j.proche.2016.03.125.
[7] Tumanski S. Handbook of magnetic measurements. 2016. https://doi.org/10.1201/b10979.
[8] Tang ZX, Lv BF. MgO nanoparticles as antibacterial agent: Preparation and activity. Brazilian J Chem Eng 2014;31:591–601. https://doi.org/10.1590/0104-6632.20140313s00002813.
[9] Hamid NA, Shamsudin NF, Seec KW. Superconducting properties and mechanical strength of MgO fibres reinforced bulk Bi-2212 superconductor ceramics. Mater Res Innov 2009;13:379–81. https://doi.org/10.1179/143307509X441612.
[10] Tang ZX, Fang XJ, Zhang ZL, Zhou T, Zhang XY, Shi LE. Nanosize MgO as antibacterial agent: Preparation and characteristics. Brazilian J Chem Eng 2012;29:775–81. https://doi.org/10.1590/S0104-66322012000400009.
[11] Dahmardeh A, Davarpanah AM. Short Communication Investigation on Influences of Synthesis Methods on the Magnetic Properties of Trimetallic Nanoparticles of Iron-Cobalt- Manganese Supported by Magnesium Oxide 2015;11:249–56.
[12] Erwin SC, Zu L, Haftel MI, Efros AL, Kennedy TA, Norris DJ. Doping semiconductor nanocrystals. Nature 2005;436:91–4. https://doi.org/10.1038/nature03832.
[13] Sharma U, Jeevanandam P. Synthesis of Zn2+-doped MgO nanoparticles using substituted brucite precursors and studies on their optical properties. J Sol-Gel Sci Technol 2015;75:635–48. https://doi.org/10.1007/s10971-015-3734-0.
[14] Vasanthi V, Kottaisamy M, Anitha K, Ramakrishnan V. Near UV excitable yellow light emitting Zn doped MgO for WLED application. Superlattices Microstruct 2017;106:174–83. https://doi.org/10.1016/j.spmi.2017.03.050.
[15] Lee JW, Ko JH. Defect states of transition metal-doped MgO for secondary electron emission of plasma display panel. J Inf Disp 2014;15:157–61. https://doi.org/10.1080/15980316.2014.955140.
[16] Azzaza S, El-Hilo M, Narayanan S, Judith Vijaya J, Mamouni N, Benyoussef A, et al. Structural, optical and magnetic characterizations of Mn-doped MgO nanoparticles. Mater Chem Phys 2014;143:1500–7. https://doi.org/10.1016/j.matchemphys.2013.12.006.
[17] Fox GT, Wolfmeyer MW, Dillinger JR, Huber DL. Magnetic field dependence of the thermal conductivity of doped MgO. Phys Rev 1968;165:898–901. https://doi.org/10.1103/PhysRev.165.898.
[18] Cai Y, Wu D, Zhu X, Wang W, Tan F, Chen J, et al. Sol-gel preparation of Ag-doped MgO nanoparticles with high efficiency for bacterial inactivation. Ceram Int 2017;43:1066–72. https://doi.org/10.1016/j.ceramint.2016.10.041.
[19] Peng L, Wang Y, Wang Z, Dong Q. Multiplesite structure and photoluminescence properties of Eu3+ doped MgO nanocrystals. Appl Phys A Mater Sci Process 2011;102:387–92. https://doi.org/10.1007/s00339-010-6027-z.
[20] Hassnain Jaffari G, Tahir A, Bah M, Ali A, Bhatti AS, Shah SI. Study of Surface-Active Modes and Defects in Single-Phase Li-Incorporated MgO Nanoparticles. J Phys Chem C

2015;119:28182–9. https://doi.org/10.1021/acs.jpcc.5b10131.
[21] Wang F, Pang Z, Lin L, Fang S, Dai Y, Han S. Magnetism in undoped MgO studied by density functional theory. Phys Rev B - Condens Matter Mater Phys 2009;80:1–7. https://doi.org/10.1103/PhysRevB.80.144424.
[22] Martínez-Boubeta C, Beltrán JI, Balcells L, Konstantinović Z, Valencia S, Schmitz D, et al. Ferromagnetism in transparent thin films of MgO. Phys Rev B - Condens Matter Mater Phys 2010;82:1–7. https://doi.org/10.1103/PhysRevB.82.024405.
[23] Hanish HH, Edrees SJ, Shukur MM. The effect of transition metals incorporation on the structural and magnetic properties of magnesium oxide nanoparticles. Int J Eng Trans A Basics 2020;33:647–56. https://doi.org/10.5829/IJE.2020.33.04A.16.
[24] Xue D, Chai G, Li X, Fan X. Effects of grain size distribution on coercivity and permeability of ferromagnets. J Magn Magn Mater 2008;320:1541–3. https://doi.org/10.1016/j.jmmm.2008.01.004.
[25] Beltrán JI, Muñoz MC, Hafner J. Structural, electronic and magnetic properties of the surfaces of tetragonal and cubic HfO2. New J Phys 2008;10. https://doi.org/10.1088/1367-2630/10/6/063031.
[26] Gallego S, Beltrán JI, Cerdá J, Muñoz MC. Magnetism and half-metallicity at the O surfaces of ceramic oxides. J Phys Condens Matter 2005;17. https://doi.org/10.1088/0953-8984/17/43/L04.
[27] Beltrán JI, Monty C, Balcells L, Martínez-Boubeta C. Possible d0 ferromagnetism in MgO. Solid State Commun 2009;149:1654–7. https://doi.org/10.1016/j.ssc.2009.06.044.
[28] Nassar MY, Mohamed TY, Ahmed IS, Samir I. MgO nanostructure via a sol-gel combustion synthesis method using different fuels: An efficient nano-adsorbent for the removal of some anionic textile dyes. J Mol Liq 2017;225:730–40. https://doi.org/10.1016/j.molliq.2016.10.135.
[29] Jeevanandam P, Klabunde KJ. A study on adsorption of surfactant molecules on magnesium oxide nanocrystals prepared by an aerogel route. Langmuir 2002;18:5309–13. https://doi.org/10.1021/la0200921.
[30] Li WC, Lu AH, Weidenthaler C, Schüth F. Hard-templating pathway to create mesoporous magnesium oxide. Chem Mater 2004;16:5676–81. https://doi.org/10.1021/cm048759n.
[31] Type D. Nucleophilic Chemistry of the Synthesized Magnesium Oxide (Magnesia) Nanoparticles via Microwave @ sol-gel Process for Removal of Sulfurous Pollutant 2020:8–10.
[32] Zaidi B, Belghit S, Ullah MS, Hadjoudja B, Guerraoui A, Gagui S, et al. Investigation of MgO powders synthesized by liquid-phase method. Metallofiz i Noveishie Tekhnologii 2019;41:1121–6. https://doi.org/10.15407/mfint.41.08.1121.
[33] Ganapathi Rao K, Ashok C, Venkateswara Rao K, Shilpa Chakra C. Structural properties of MgO Nanoparticles: Synthesized by Co-Precipitation Technique. Int J Sci Res 2013:43–6.
[34] Mohammad Shafiee MR, Kargar M, Ghashang M. Characterization and low-cost, green synthesis of Zn2+ doped MgO nanoparticles. Green Process Synth 2018;7:248–54. https://doi.org/10.1515/gps-2016-0219.
[35] Ghorbani S, Razavi RS, Loghman-Estarki MR, Alhaji A. Development of MgO–Y2O3 Composite Nanopowder by Pechini Sol–Gel Method: Effect of Synthesis Parameters on Morphology, Particle Size, and Phase Distribution. J Clust Sci 2017;28:1523–39. https://doi.org/10.1007/s10876-017-1162-8.
[36] Tai CY, Tai C Te, Chang MH, Liu HS. Synthesis of magnesium hydroxide and oxide nanoparticles using a spinning disk reactor. Ind Eng Chem Res 2007;46:5536–41. https://doi.org/10.1021/ie060869b.
[37] Pechini MP. (Enno&P and Alway 1967.
[38] Zalapa-Garibay MA, Arizmendi-Moraquecho A, Reyes-López SY. Low temperature synthesis of alpha alumina platelets and acicular mullite in MgO-Al 2 O 3 -SiO 2 system. J Ceram Sci Technol 2019;10:9–18. https://doi.org/10.4416/JCST2018-00043.
[39] Devaraja PB, Avadhani DN, Nagabhushana H, Prashantha SC, Sharma SC, Nagabhushana BM, et al. Luminescence properties of MgO: Fe 3+ nanopowders for WLEDs under NUV excitation prepared via propellant combustion rout e . J Radiat Res Appl Sci 2015;8:362–73. https://doi.org/10.1016/j.jrras.2015.02.001.

[40] Obeid MM, Edrees SJ, Shukur MM. Synthesis and characterization of pure and cobalt doped magnesium oxide nanoparticles: Insight from experimental and theoretical investigation. Superlattices Microstruct 2018;122:124–39. https://doi.org/10.1016/j.spmi.2018.08.015.
[41] Leszczyński M, Litwin-Staszewska E, Suski T, Bąk-Misiuk J, Domagała J. Lattice Constant of Doped Semiconductor. Acta Phys Pol A 1995;88:837–40. https://doi.org/10.12693/aphyspola.88.837.
[42] Rajesh Kumar B, Hymavathi B. X-ray peak profile analysis of solid-state sintered alumina doped zinc oxide ceramics by Williamson–Hall and size-strain plot methods. J Asian Ceram Soc 2017;5:94–103. https://doi.org/10.1016/j.jascer.2017.02.001.
[43] Zhang L, Gonçalves AAS, Jaroniec M. Identification of preferentially exposed crystal facets by X-ray diffraction. RSC Adv 2020;10:5585–9. https://doi.org/10.1039/d0ra00769b.
[44] Ansari A, Ali A, Asif M, Shamsuzzaman. Microwave-assisted MgO NP catalyzed one-pot multicomponent synthesis of polysubstituted steroidal pyridines. New J Chem 2018;42:184–97. https://doi.org/10.1039/c7nj03742b.
[45] Das A, Mandal AC, Roy S, Nambissan PMG. Internal defect structure of calcium doped magnesium oxide nanoparticles studied by positron annihilation spectroscopy. AIP Adv 2018;8. https://doi.org/10.1063/1.5001105.
[46] Theophanides T. Introduction to Infrared Spectroscopy. Infrared Spectrosc - Mater Sci Eng Technol 2012. https://doi.org/10.5772/49106.
[47] Elawam S, Morsi W, Abou-Shady H, Guirguis O. Characterizations of Beta-lead Oxide "Massicot" Nano-particles. Br J Appl Sci Technol 2016;17:1–10. https://doi.org/10.9734/bjast/2016/28143.
[48] Scimeca M, Bischetti S, Lamsira HK, Bonfiglio R, Bonanno E. Energy dispersive X-ray (EDX) microanalysis: A powerful tool in biomedical research and diagnosis. Eur J Histochem 2018;62:89–99. https://doi.org/10.4081/ejh.2018.2841.
[49] Li M, Zhou S, Xu M. Graphene oxide supported magnesium oxide as an efficient cathode catalyst for power generation and wastewater treatment in single chamber microbial fuel cells. Chem Eng J 2017;328:106–16. https://doi.org/10.1016/j.cej.2017.07.031.
[50] Morozov IG, Sathasivam S, Belousova O V., Parkin IP, Kuznetcov M V. Effect of synthesis conditions on room-temperature ferromagnetic properties of Mg-O nanoparticles. J Alloys Compd 2018;765:343–54. https://doi.org/10.1016/j.jallcom.2018.06.211.
[51] Ferrari AM, Pacchioni G. Electronic structure of F and V centers on the MgO surface. J Phys Chem 1995;99:17010–8. https://doi.org/10.1021/j100046a029.
[52] Elfimov IS, Yunoki S, Sawatzky GA. Possible Path to a New Class of Ferromagnetic and Half-Metallic Ferromagnetic Materials. Phys Rev Lett 2002;89:1–4. https://doi.org/10.1103/PhysRevLett.89.216403.
[53] Kumar A, Kumar J, Priya S. Defect and adsorbate induced ferromagnetic spin-order in magnesium oxide nanocrystallites. Appl Phys Lett 2012;100. https://doi.org/10.1063/1.4712058.
[54] Freund MM, Freund F, Batllo F, Field M. Highly Mobile Oxygen Holes in Magnesium Oxide 1989;V:1–4.
[55] Singh JP, Gautam S, Srivastava RC, Asokan K, Kanjilal D, Chae KH. Crystallite size induced crossover from paramagnetism to superparamagnetism in zinc ferrite nanoparticles. Superlattices Microstruct 2015;86:390–4. https://doi.org/10.1016/j.spmi.2015.07.062.